A Mesoproterozoic iron formation

Donald E. Canfield[a,b,1], Shuichang Zhang[a], Huajian Wang[a], Xiaomei Wang[a], Wenzhi Zhao[a], Jin Su[a], Christian J. Bjerrum[c], Emma R. Haxen[c], and Emma U. Hammarlund[b,d]

[a]Research Institute of Petroleum Exploration and Development, China National Petroleum Corporation, 100083 Beijing, China; [b]Institute of Biology and Nordcee, University of Southern Denmark, 5230 Odense M, Denmark; [c]Department of Geosciences and Natural Resource Management, Section of Geology, University of Copenhagen, 1350 Copenhagen, Denmark; and [d]Translational Cancer Research, Lund University, 223 63 Lund, Sweden

Contributed by Donald E. Canfield, February 21, 2018 (sent for review November 27, 2017; reviewed by Andreas Kappler and Kurt O. Konhauser)

We describe a 1,400 million-year old (Ma) iron formation (IF) from the Xiamaling Formation of the North China Craton. We estimate this IF to have contained at least 520 gigatons of authigenic Fe, comparable in size to many IFs of the Paleoproterozoic Era (2,500–1,600 Ma). Therefore, substantial IFs formed in the time window between 1,800 and 800 Ma, where they are generally believed to have been absent. The Xiamaling IF is of exceptionally low thermal maturity, allowing the preservation of organic biomarkers and an unprecedented view of iron-cycle dynamics during IF emplacement. We identify tetramethyl aryl isoprenoid (TMAI) biomarkers linked to anoxygenic photosynthetic bacteria and thus phototrophic Fe oxidation. Although we cannot rule out other pathways of Fe oxidation, iron and organic matter likely deposited to the sediment in a ratio similar to that expected for anoxygenic photosynthesis. Fe reduction was likely a dominant and efficient pathway of organic matter mineralization, as indicated by organic matter maturation by Rock Eval pyrolysis combined with carbon isotope analyses: Indeed, Fe reduction was seemingly as efficient as oxic respiration. Overall, this Mesoproterozoic-aged IF shows many similarities to Archean-aged (>2,500 Ma) banded IFs (BIFs), but with an exceptional state of preservation, allowing an unprecedented exploration of Fe-cycle dynamics in IF deposition.

oxygen | banded iron formation | anoxygenic photosynthesis | Mesoproterozoic | green sulfur bacteria

Iron formations (IFs) are Fe-enriched sedimentary rocks found in relative abundance between ∼3,000 and 1,800 million years ago (Ma), and again ∼800 Ma, but they are very scarce in the billion years in between (1–4). As IFs are composed of minerals thought to have ultimately derived from Fe(II)-containing marine waters (e.g., refs. 1 and 5), the lack of Fe formations between 1,800 and 800 Ma implies a lack of abundant seawater Fe(II) during this time interval. There have been two proposals to account for a lack of Fe(II). In one suggestion, atmospheric oxygen concentrations increased to levels sufficient to oxygenate the deep ocean, thus removing Fe(II) through oxidation (5). In another suggestion, Fe(II) was, instead, removed through precipitation by sulfide (6). In the latter scenario, an increase in sulfate flux to the ocean followed the great oxidation of the atmosphere (GOE) some 2,300 Ma (5, 7, 8). An increase in sulfate availability increased rates of sulfate reduction in a dominantly anoxic ocean, removing Fe(II) from solution (7). Recent work has uncovered substantial amounts of ocean anoxia in the time window between 1,800 and 800 Ma (9–17), thus possibly favoring the second scenario. However, anoxic waters were frequently ferruginous, and thus, the lack of IFs between 1,800 and 800 Ma remains enigmatic.

Apart from issues related to the abundance of IFs through time, there is still much debate on the mechanisms of IF deposition (18–24). IFs comprise a variety of different minerals including Fe oxides, Fe sulfides, Fe silicates, and Fe carbonates (e.g., refs. 1, 25, and 26), and there is much discussion about which of these phases are primary precipitates and which are secondary minerals (e.g., refs. 1 and 27–30). There is also a broader debate as to how these minerals formed and the possible role of biology in their genesis (e.g., refs. 1, 3, 21, and 31–33).

Understanding the genesis of the Fe minerals in IFs is one step toward understanding the relationship between IFs and the chemical and biological environment in which they formed. For example, the high Fe oxide content of many IFs (e.g., refs. 32, 34, and 35) is commonly explained by a reaction between oxygen and Fe(II) in the upper marine water column, with Fe(II) sourced from the ocean depths. The oxygen could have come from exchange equilibrium with oxygen in the atmosphere or from elevated oxygen concentrations from cyanobacteria at the water-column chemocline (e.g., refs. 1, 3, 31, and 32). The oxidation could have been strictly inorganic, given the rapid reaction kinetics between Fe(II) and oxygen (36, 37), or it could have been mediated by aerobic Fe(II)-oxidizing prokaryotes like *Mariprofundus* sp. (e.g., ref. 38). Indeed, there is some evidence that biological oxidation is favored over inorganic oxidation at low oxygen concentrations (39).

Another possible route of iron oxide formation is the oxidation of Fe(II) to iron oxyhydroxides by bacterial anoxygenic photosynthesis. Notably, this pathway does not require oxygen. Anoxygenic photosynthesis was first proposed by refs. 18 and 19 as having a possible role in IF formation, and the anoxygenic phototrophic oxidation of Fe(II) was subsequently discovered as a prokaryote metabolism by ref. 20. Since then, anoxygenic photosynthetic oxidation of Fe(II) has been found among both purple nonsulfur and green sulfur bacterial lineages (e.g., ref. 40), and these bacteria have been found active in modern ferruginous settings (41, 42). These observations support the idea that anoxygenic photosynthesis could have driven Fe(II) oxidation in ancient IF settings (e.g., refs. 18–24). Still, despite these

Significance

Iron formations (IFs) are common before 1,800 million years ago (Ma) and again at ∼750 Ma, but are remarkably absent for the billion years in between. We report on a 1,400-Ma IF of ∼520 gigatons Fe from the Xiamaling Formation on the North China Craton. Biomarker analyses suggest that anoxygenic phototrophic bacteria were involved in Fe(II) oxidation, and further geochemical analysis shows that IF sediments supported active microbial Fe reduction that rivaled oxic respiration in its efficiency of organic matter oxidation. The Xiamaling Formation IF demonstrates that geochemical conditions occasionally conspired to produce world-class IFs during Earth's "middle ages," permitting critical insights into the biogeochemical processes of IF emplacement.

Author contributions: D.E.C., S.Z., H.W., X.W., E.R.H., and E.U.H. designed research; D.E.C., S.Z., H.W., X.W., W.Z., J.S., C.J.B., E.R.H., and E.U.H. performed research; S.Z. contributed new reagents/analytic tools; D.E.C., S.Z., H.W., X.W., J.S., C.J.B., E.R.H., and E.U.H. analyzed data; and D.E.C., S.Z., X.W., C.J.B., E.R.H., and E.U.H. wrote the paper.

Reviewers: A.K., University of Tuebingen; and K.O.K., University of Alberta.

The authors declare no conflict of interest.

[1]To whom correspondence should be addressed. Email: dec@biology.sdu.dk.

This article contains supporting information online at www.pnas.org/lookup/suppl/doi:10.1073/pnas.1720529115/-/DCSupplemental.

Published online April 9, 2018.

recent insights, the role of anoxygenic phototrophic bacteria in IF formation remains uncertain (43).

While many IFs are characterized by iron oxide phases, many also contain abundant, if not dominant, iron carbonates (e.g., refs. 1, 26, 28, 32, 44, and 45). These minerals precipitated either directly from the anoxic Fe(II)-containing water column or during early diagenesis in the sediments. In both cases, microbial reduction of ferric oxides produced in the upper water column would have elevated the concentration of Fe(II) as well as the pH and bicarbonate concentration, all favorable for siderite precipitation (e.g., ref. 44). However, the metabolic products of microbial respiration reactions typically accumulate to much higher concentrations in sediments compared with the water column (46), so that mineral formation driven by respiration is more favored in sediments. The carbonate associated with siderite in siderite-rich IFs is typically depleted in ^{13}C, sometimes greatly so, compared with likely values for seawater (26, 47). These large ^{13}C-depleted values are consistent with the role of Fe reduction in carbonate formation, most likely in sediments (1, 47), but without further proof, the role of Fe reduction in IF generation remains uncertain.

We report here on a substantial IF in the ∼1,400 Ma Xiamaling Formation of the North China Craton. Within the current boundaries of the Xiamaling Formation, this IF likely contained ∼520 gigatons (Gt) of authigenic Fe, placing it in the same order of magnitude as many Archean, Paleoproterozoic, and Neoproterozoic IFs (48). The Xiamaling IF also contains biomarker and geochemical evidence for a dynamic biological Fe cycle, including extensive and efficient dissimilatory Fe reduction and anoxygenic phototrophic Fe oxidation. Much of this evidence is only possible because of the low thermal maturity of the Xiamaling rocks uniquely preserving biomarkers and other organic geochemical indicators. Thus, the Xiamaling IF provides the best-resolved insights to date as to the role of the ancient Fe cycle in IF deposition and diagenesis, and during a time when IF deposition has been considered unimportant.

The Geologic Setting

The IF we describe is found within the Xiamaling Formation on the North China Craton. The Xiamaling Formation is part of the Paleoproterozoic to mid-Mesoproterozoic sedimentary succession deposited onto Paleoproterozoic crystalline rocks within the Yanliao rift (49, 50), which is one of three recognized and contemporaneous rift systems on the North China Craton. The other two rift systems are the Zhaertai-Baiyun Obo rift system to the northwest and the Xiong'er rift system to the south (Fig. 1) (49). These rifts may represent part of the early initial breakup of Supercontinent Columbia (Nuna) (50).

The sedimentary rocks of the Yanliao rift, containing the Xiamaling Formation, begin with the Changcheng Group, which represents sedimentation in an opening rift beginning some 1,700 Ma (Fig. 2) (51, 52). The overlying Nankou Group represents a transition from active rifting to a passive margin setting, which is represented by the overlying Jixian Group. The Tieling Formation, at the top of the Jixian Group, has a U-Pb age of 1,437 ± 21 Ma, obtained from zircons extracted from a K-bentonite (53). The Bilute Formation of the Zhaertai-Baiyun Obo rift system has been correlated with various sedimentary units of the Jixian Group of the Yanliao rift system (49, 50), and it is suggested that these rift systems were connected by a mix of shallow and deep marine settings until ∼1,400 Ma (49, 50). The paleogeographic details, however, are clouded by uncertainty as to the relationship between the North China Craton and the Supercontinent Columbia (Nuna) (54, 55). The Xiamaling Formation began depositing at around this time with precise thermal

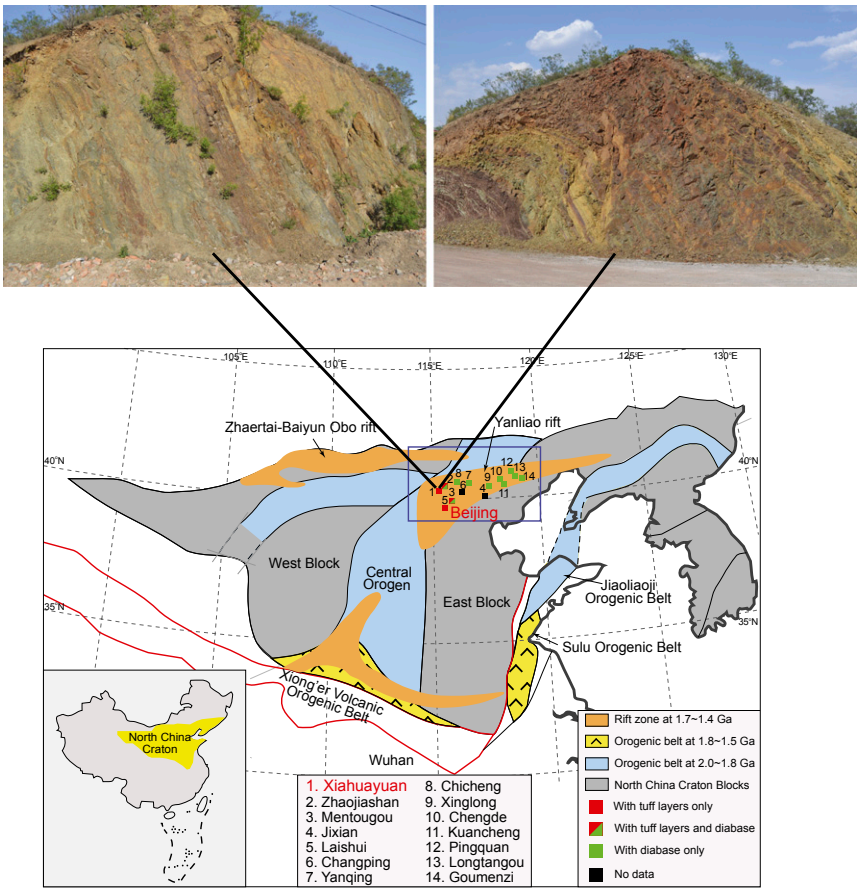

Fig. 1. Map of North China, highlighting the Yanliao rift where the Xiamaling Formation is found. Reported locations of the Xiamaling Formation are indicated. Unit 5 IF has been reported both at Xiahuayuan, where we have done our sampling, and at Jixian (see text for details). Also shown are locations of diabase activity and where tuff layers have been reported. Finally, photos show the Xiamaling IF in outcrop with lines indicating locations. In the outcrop photo in *Upper Right*, the transition between units 5 and 4 (alternating red/green sediment) is seen in the lower left of the photo.

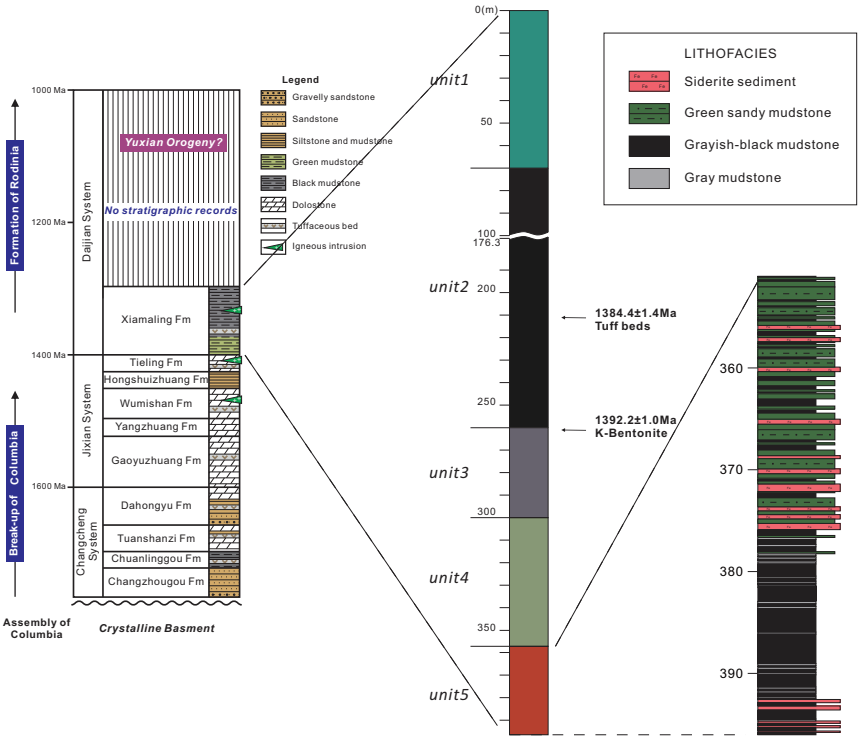

Fig. 2. Stratigraphy of unit 5, placed in the context of the Xiamaling Formation and the North China Craton. The general stratigraphic column for the North China Craton is modified from ref. 13, while detailed stratigraphic columns for units 1–4 are also found in ref. 13.

ionization mass spectrometric (TIMS) dating yielding ages of 1,384 ± 1.4 Ma for zircons from a tuff layer in unit 2 and 1,392.2 ± 1.0 Ma for a bentonite layer in unit 3 located 52 m below the tuff in stratigraphic height (56) (Fig. 2).

Some have argued that these Xiamaling Formation ash layers provide evidence for volcanism associated with subduction, thereby placing the Xiamaling Formation in an environment transiting from a passive margin setting to one experiencing the initiation of subduction in a back-arc basin setting (50). However, as we have noted previously (13), ash layers are rare in the Xiamaling Formation, as they are found in only two intervals. Furthermore, through most of its depositional history, the Xiamaling Formation deposited well-laminated sediments under quiet deep-water depositional conditions (13), including the intervals housing ash layers. Thus, the Xiamaling Formation is absent of evidence for the tectonic events delivering massive debris flows and the pervasive volcanism that might be expected in a back-arc environment. Numerous diabase dikes intercept the Xiamaling Formation at various locations (Fig. 1). These are dated to between 1,316 and 1,353 Ma (54, 55, 57), and these dikes may indicate the initiation of local rifting and the final breakup of the North China Craton from Supercontinent Columbia (Nuna) (54). Still, these events postdate the Xiamaling Formation. Overall, we believe that available evidence points to continued deposition of the Xiamaling Formation in a passive margin setting. We also highlight that the Xiamaling Formation has experienced a remarkably low degree of thermal maturity, likely never having been heated to >90 °C (56), and thus preserving, to our knowledge, the best available IF record of biomarkers and other organic biogeochemical indicators. A detailed accounting of our sampling procedures and analytical methods is found in *SI Materials and Methods*, with a compilation of all our analytical data.

The Xiamaling Formation IF

In the Xiahuayuan area, we observed the IF in outcrop at three locations, and in each case, ~12 m of Fe-containing strata were exposed (Fig. 1, showing two of the locations). We also intercepted the IF in two cores: In one core, we collected the very top the IF, while in the other core, we intercepted the IF over a depth of ~45 m. Stratigraphically, the IF-containing interval of the Xiamaling Formation comprises unit 5 of our informal classification scheme (Fig. 2) (13). We defined the top of unit 5 as the transition between the overlying red–green layers of unit 4 (13) and the underlying ferruginous sediments as clearly seen in both core and outcrop (Fig. 1). The lower part of unit 5 was not observed in outcrop, and we took the bottom of the unit as the bottom of our deepest core, recognizing that Fe-enriched sediments could extend even deeper into the subsurface.

Sedimentation in unit 5 is complex. Sedimentary fabrics range from laminated silty muds (Fig. 3*A*), indicative of a simple (hemi)pelagic settling, to thin event beds (Fig. 3*B*) and cross-bedded fabrics (Fig. 3*C*), indicative of active sediment transport and possible current influence. Also common are signs of sediment deformation, erosion, slump scars, and active sediment mobilization (Fig. 3*D*). These fabrics are consistent with liquification and gravity-driven deformation, possibly due to sediment loading or seismic shocks. Overall, unit 5 was an active depositional environment, with the deposition of background muds interrupted by mass flows, bottom currents, and postdepositional disturbance. Despite this, there is no indication of cross-laminated features consistent with wave impingement on the sediments, and thus, the sediments likely deposited well below storm wave base.

Iron enrichments in unit 5 are concentrated in the upper 25 m of the unit (Figs. 2 and 4) and in the lower 5 m (Fig. S1 showing the lower Fe-enriched region, where we have limited geochemical data). The Fe enrichments are not uniform, where the most enriched sediments are composed of layers of <1 cm to several-centimeter thickness as revealed through visual inspection and through 0.1-mm resolution core scanning with X-ray fluorescence (μXRF) (Fig. S2). When associated with a high clastic load, Fe is enriched in secondary Fe-silicate phases like glauconite, with occasional siderite cement (Fig. 3*E*). As the clastic load decreases, the siderite content increases, and the most Fe-enriched layers are composed of densely packed siderite rhombs (Fig. 3*F*), with siderite also a dominant phase in X-ray diffraction (XRD) (Fig. S3).

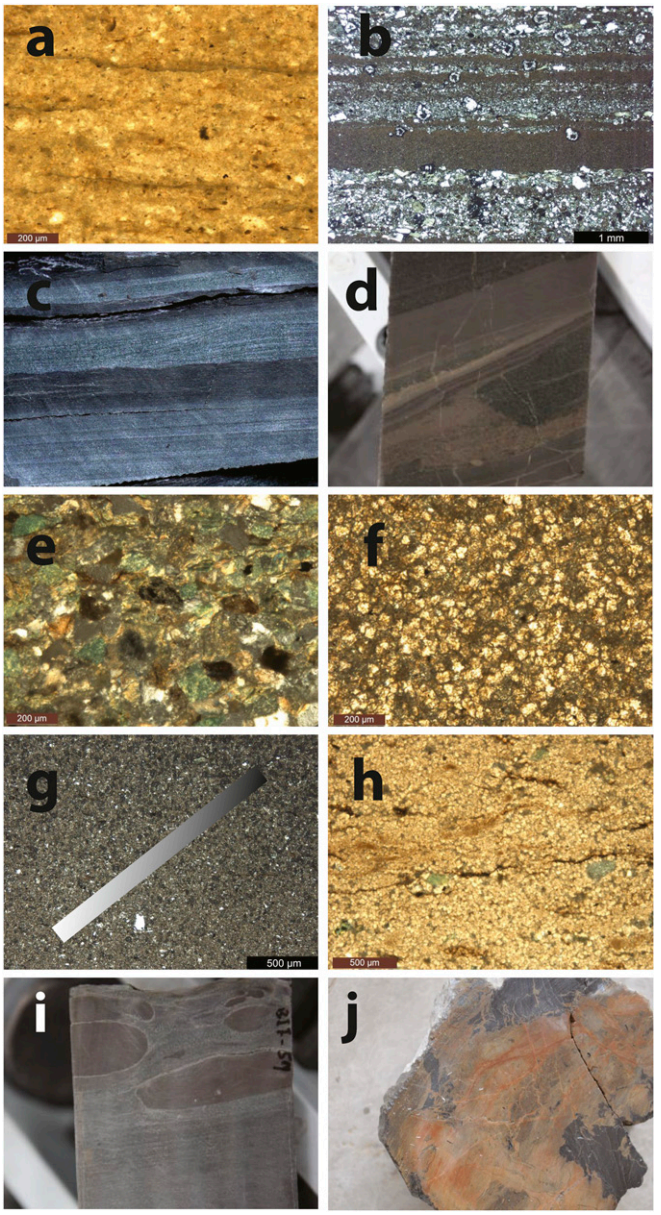

Fig. 3. Photos and photomicrographs of unit 5. (*A*) Background sedimentation of silty mud showing some evidence of weak lamination. (*B*) Microscopic event beds in a background of mudstone. (*C*) Cross-laminated silty and fine-grained sandy event beds. (*D*) IF (brown) in complex matrix with signs of sediment deformation with erosional features. Also shown is possible mobilization and possible injection of Fe-rich sediment around an apparent muddy clast. (*E*) Fe-enriched sands with abundant secondary Fe-enriched sheet silicates. (*F*) Densely packed siderite in a conspicuous IF layer. (*G*) Detrital silts with gradient in siderite content, where the gradient direction is shown with the inserted rectangle. (*H*) Densely packed siderite with weak laminations (possibly organic matter) and large grains of secondary mica. (*I*) Siderite layer showing evidence of mobilization and possible plastic deformation. (*J*) Bottom IF layer showing evidence of brittle deformation.

The transition between Fe-poor and Fe-enriched layers can be gradual (Fig. 3*G*), and frequently, the Fe-enriched layers show evidence of microlaminations (Fig. 3*H*), possibly due to layers of organic matter deposition. The highly Fe-enriched layers can also be unlaminated and can show evidence of mobilization and even injection into adjacent clastic sediments (Fig. 3 *D* and *I*), displaying features consistent with plastic deformation. The deepest Fe layers are chaotic, showing clear evidence of mixing, reworking, and brittle fracture (Fig. 3*J*). We cannot be certain, but this deep layer appears to have been mobilized and transported in a semisolid state, possibly due to seismic activity after partial solidification. We have not, however, conducted a full geochemical survey of this deeper Fe layer, so this layer will not be further discussed.

Altogether, the Xiamaling Formation IF is not a banded IF (BIF), as it lacks the characteristic laminations. Nor is it a typical granular IF (GIF), as it is not oolitic, and the iron grains do not show evidence of pervasive transport in a high-energy environment (e.g., ref. 1). Observations do, however, support IF accumulation through chemical sedimentation from the water column with sedimentological and diagenetic (as explored in detail below) reworking of the original Fe phases.

What appear to be similar Fe-enriched layers have also been reported in the Jixian region, some 200 km to the East of our sampling location (58–60) (Fig. 1). These deposits, too, seem to extend over a depth interval of tens of meters (60), although they have not been explored in detail.

Size of the IF

As described above, chemical analysis reveals numerous peaks in iron concentration to values between 20 and 33 wt% Fe in the upper 25 m of unit 5, with highly Fe-enriched layers extending in thickness from <1 cm to several centimeters (Fig. 4 and Figs. S1 and S2). Overall, however, Fe concentrations are elevated over the crustal average concentration of 3.5 wt% in the whole of the upper Fe-enriched zone of the IF, located between 350 and 376 m (Fig. 2). Between 376 and 390 m, iron concentrations are close to the crustal average value, with an increase in the bottom 4 m of the core to values as high as 47 wt%, but with background concentrations also near the crustal average (Fig. S1). We note that in the Jixian region, total Fe concentrations of up to 41.6 wt% were measured (60).

With these data, we estimate the amount of IF-associated Fe in unit 5 of the Xiamaling Formation. The average concentration of Fe over the 44 m of unit 5 is 10.8 wt%. Subtracting the crustal average concentration of 3.5 wt% yields an excess Fe concentration of 7.3 wt%. We measured an average sediment density for the core sections scanned in Fig. S2 of 2.7 $g{\cdot}cm^{-3}$, which generates an Fe load of 8.7×10^2 $g{\cdot}cm^{-2}$ over the 44 m of unit 5. If we assume this same Fe load over the whole of the 60,000 km^2 of Xiamaling Formation, we obtain a total of 520 Gt Fe. We do not know the whole areal or vertical extent of the Xiamaling IF, but the description of a significant Xiamling IF some 200 km from our location (58–60) (Fig. 1) gives us confidence that the Xiamaling Formation IF was quite substantial when deposited, and that our estimate of Fe load is likely in the right order of magnitude.

While an IF of 520 Gt is much smaller than the massive (10,000–100,000 Gt), and best-known, IFs of the Neoarchean Eon (2,800–2,500 Ma), it is comparable in size to a host of IFs deposited between 2,000 and 2,400 Ma and is by far the largest reported IF for the billion years between 1,800 and 800 Ma (48). Thus, the Mesoproterozoic Era (1,600–1,000 Ma) is not devoid of significant IF deposition as once thought (e.g., refs. 1, 2, and 48). Rather, it appears that ferruginous conditions, apparently common in Mesoproterozoic ocean water (10, 17, 37), at least occasionally conspired to produce an IF of considerable size. We explore the availability of Fe(II) for IF deposition in more detail below.

The Depositional Environment and Source of Fe

As noted above, the Xiamaling Formation IF deposited in a setting with occasional bottom currents and mass flows, but it also likely deposited below storm wave base, at least in the location of our sediment cores. The Fe enrichments themselves

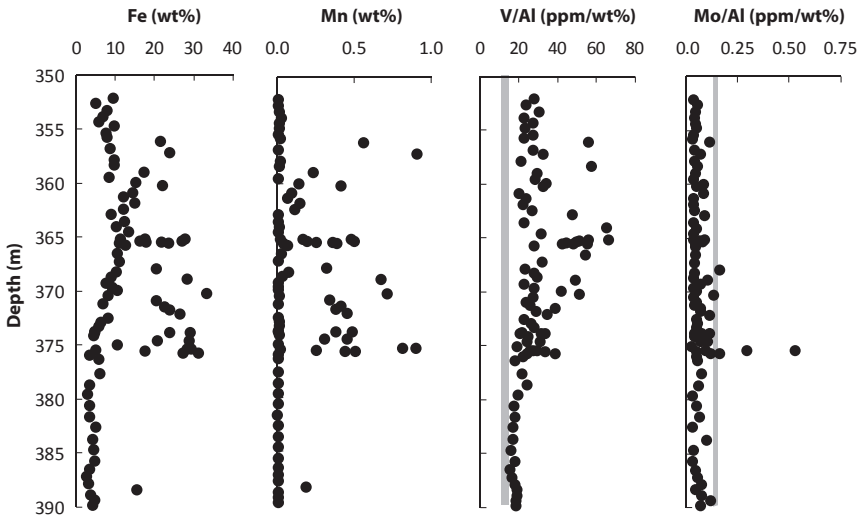

Fig. 4. Fe, Mn, and trace element data for the upper IF of unit 5 and the underlying sands and silts. The lowermost IF is not included (see Fig. S1 for Fe concentrations). The gray bars show crustal average values for V/Al and Mo/Al, with crustal averages from ref. 98.

(Fig. 5 and Fig. S1) speak to anoxic bottom water conditions. Such conditions would also explain enrichments in vanadium, as the vanadate ion $[VO_2(OH)_3^{2-}$, V(V)] is reduced to immobile V (IV) and V(III) phases under reducing conditions (61). Rare Earth element (REE) plus yttrium patterns are also used to assess depositional environment. In this case, a shale-normalized negative Ce anomaly is usually taken to indicate deposition in oxygenated environments, as oxygenated seawater contains strong negative Ce anomalies (62). Our samples, and particularly our high-Fe samples, which should contain the greatest authigenic REE plus yttrium complement, show no Ce anomaly (Figs. S3 and S4). This is typical for IFs (43, 63–65), and it is also consistent with Fe deposition from an anoxic environment. Molybdenum, in contrast, is not generally enriched above crustal average values (Fig. 5), as might be expected in a low-sulfide environment (66, 67). Enrichments in Mn correlate with Fe enrichments (Fig. 5 and Fig. S2), demonstrating, as is typical for IFs, the co-occurrence (and removal) of Fe and Mn in basin waters where the IFs precipitated (26, 68–70).

We measured the presence of 2,3,6-trimethyl aryl isoprenoids (2,3,6-TMAIs) through most of the unit (Fig. 5, showing the C-18 and -19 TMAIs). We believe these TMAIs to be indigenous based on analysis of inside and outside pieces of core (71) (*SI Materials and Methods*). The TMAIs are particularly abundant in the Fe-rich layers at ∼365 and ∼375 m, but their overall abundance is some 10 times lower than measured previously in overlying units of the Xiamaling Formation (13, 72). The 2,3,6-TMAI biomarkers are breakdown products of the carotenoid pigments of "brown" strains of anoxygenic phototrophic green sulfur bacteria (GSBs). Their presence, therefore, is typically ascribed to the presence of an anoxygenic phototrophic population in an anoxic water-column setting (73, 74).

A formation pathway for 2,3,6-TMAIs from the β-carotene of cyanobacteria and algae, however, has also been identified (75). We previously argued that the TMAIs in unit 3 of the Xiamaling Formation were likely derived from GSBs (72). Our argument was based on positive whole-rock carbon isotope excursions in association with peak 2,3,6-TMAI abundance, where GSBs produce relatively ^{13}C-enriched organic matter through carbon

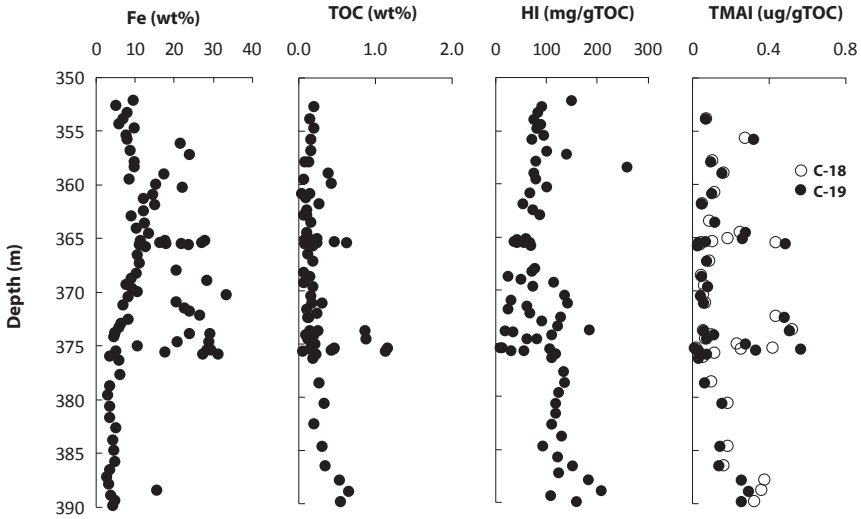

Fig. 5. The concentration of total Fe together with various organic geochemical parameters for unit 5 of the Xiamaling Formation.

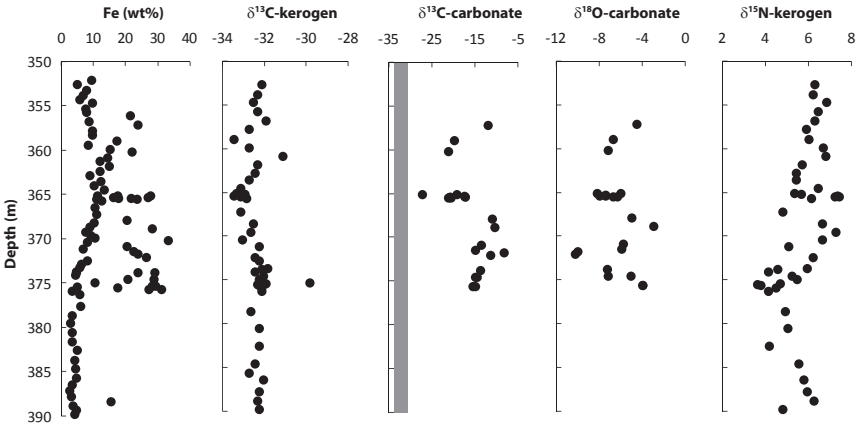

Fig. 6. The concentration of total Fe together with the $\delta^{13}C$ and $\delta^{15}N$ of kerogen as well as the $\delta^{13}C$ and $\delta^{18}O$ of carbonates from unit 5 of the Xiamaling Formation. The gray field in the $\delta^{13}C$-carbonate plot indicates the range of $\delta^{13}C$-kerogen values.

fixation by the reductive citric acid cycle (reviewed in ref. 76). We see no positive isotope shifts in the elevated TMAI intervals of unit 5 (Figs. 5 and 6), but the TMAI concentrations are very low, and such a shift might not be expected. Therefore, by analogy with unit 3, we cautiously suggest that the 2,3,6-TMAIs demonstrate the presence of an ancient population of GSBs at the chemocline in the water column during deposition of unit 5, especially during periods of high Fe deposition. GBSs conduct both the phototrophic oxidation of H_2S (77) and Fe(II) (78), but due to the great abundance of Fe carbonates, and the low abundance of sulfides in this unit [undetected by XRD, even after siderite removal; Fig. S3], we argue that the GSBs of unit 5 would have most likely been active in the oxidation of Fe(II).

Neither Fe enrichments nor trace metals provide compelling evidence for anoxic depositional conditions in the low-Fe interval between 377 and 390 m in the core (Fig. 4). However, the presence of 2,3,6-TMAIs in this interval, and the associated activity of anoxygeneic phototrophs, argue for at least intermittent anoxic conditions during the deposition of the unit (Fig. 5).

As mentioned, IFs are rare in the time interval between 1,800 and 800 Ma; therefore, the Xiamaling IF required a source of Fe(II) well in excess of normal for marine depositional environments during this time. It is often argued, based on REE (plus yttrium) patterns, and in particular positive Eu anomalies, that the Fe(II) for IF deposition originated from hydrothermal sources (1, 43, 63, 65). This is because hydrothermal fluids carry a positive Eu anomaly (79), and they are also typically Fe(II) enriched (80). Thus, periods of elevated IF deposition have been linked to periods of enhanced mantle plume activity as evidenced by the emplacement of large igneous provinces and major periods of dike swarm activity (4). REE (plus yttrium) patterns for unit 5 of the Xiamaling Formation show a positive, but relatively small, Eu anomaly in the high-Fe sections ($Eu/Eu^* < 1.2$) (Figs. S3 and S4). This rather muted Eu anomaly follows a general trend of reduced Eu anomalies in going from IFs deposited in the Archean Eon ($Eu/Eu^* = 1.2–4.5$) to the Neoproterozoic Era ($Eu/Eu^* = 1–1.4$) (43). Thus, while there may have been a hydrothermal contribution to the Fe precipitating with Xiamaling Formation IF, its magnitude is difficult to constrain and may have been small.

While the Xiamaling IF is restricted to unit 5 of the Xiamaling Formation, ferruginous depositional conditions were common through the whole of Xiamaling Formation deposition. Thus, moving up section, the IF of unit 5 transits rather abruptly into the organic-poor (0.07–0.2 wt%) red–green muddy silts of unit 4 (13) (Fig. 1). The red layers of unit 4 also deposited under ferruginous conditions (13), but the sediment Fe concentrations are much lower than in the unit 5 IF (mostly <7 wt% Fe except in the 3 m above unit 5 where they reach 13.7 wt%; ref. 13). Therefore, we can speculate that water-column Fe(II) concentrations were also much lower during unit 4 deposition. In any case, it appears that ferruginous conditions continued after the transition from unit 5 to 4, but unit 4 represents a very different depositional environment that we have previously interpreted as a low-productivity ferruginous oxygen-minimum zone (13). Ferruginous conditions may have also dominated the oxygen-minimum zone recorded in unit 3 (13, 72) as well as the lower part of unit 2 (13). Overall, ferruginous conditions were common during Xiamaling Formation deposition, but only in unit 5 were Fe deposition rates high enough to form an IF of substantial proportions—indeed, larger than anything else known in the Mesoproterozoic Era.

As noted above, IF deposition in unit 5 has been spurred by an enhanced hydrothermal Fe source, but we cannot rule out other possibilities. For example, an enhanced Fe flux could have accompanied high rates of upwelling of Fe(II)-containing waters, or, alternatively, an enhanced sediment source of Fe(II), possibly related to reduced seawater sulfate concentrations (37). With the present evidence, we cannot be sure.

Fe Cycling

From both petrographic observations (Fig. 3 *E–H*) and XRD results (Fig. S5), the iron oxide content of the upper iron-enriched layers of unit 5 is extremely low. Thus, by far most of the enriched iron was present as siderite or as iron-silicate phases in the clastic-rich intervals (Fig. 3*E*). The carbonate associated with the siderite is highly depleted in ^{13}C, with $\delta^{13}C$ values ranging from approximately −8 to −28‰ (Fig. 6). These values, especially the lighter ones, are extremely depleted, even compared with other siderite IFs, where siderites from the late Archean Transvaal Supergroup, South Africa have minimum values of −12 to −15‰ (47, 81, 82), as do siderites from the similarly aged Brockman Iron Formation, Hamersley Basin, Australia (83).

All of these isotopically depleted siderites, including those from the Archean Eon, can be explained by the incorporation of carbonate produced from organic matter respiration, as organic matter is also ^{13}C-depleted (43, 47, 81, 82). Since IFs typically contain little sulfide, and thus show little evidence for significant sulfate reduction, Fe oxides are considered the most likely electron acceptor for organic matter respiration (43, 82, 83), although methanogenesis has also been proposed (24). It has been argued that during Fe reduction (Eq. **1**), ^{18}O-depleted oxygen from the iron oxides can be transferred to the carbonate being produced,

generating ^{18}O-depleted siderites whose isotopic composition generally follows that of the carbonate carbon (82). Such a trend was seen in Archean siderite BIFs (82), and is also seen in unit 5 of the Xiamaling Formation (Fig. 6).

With these processes in mind, a general cartoon of the Fe and carbon cycles in the Xiamaling IF is presented in Fig. 7. Iron oxides can form either through the oxidation of dissolved Fe^{2+} at the chemocline with oxygen (Eq. **2**) or from anoxygenic photosynthesis (Eq. **3**).

$$4Fe(OH)_3 + CH_2O + 7H^+ \rightarrow 10H_2O + 4Fe^{2+} + HCO_3^-. \quad [1]$$

$$10H_2O + 4Fe^{2+} + O_2 \rightarrow 4Fe(OH)_3 + 8H^+. \quad [2]$$

$$10H_2O + 4Fe^{2+} + HCO_3^- \rightarrow 4Fe(OH)_3 + CH_2O + 7H^+. \quad [3]$$

$$HCO_3^- + H^+ \rightarrow CH_2O + O_2. \quad [4]$$

$$4Fe^{2+} + 4HCO_3^- \rightarrow 4FeCO_3 + 4H^+. \quad [5]$$

If the oxygen used to oxidize Fe(II) (Eq. **2**) is derived from oxygenic photosynthesis (Eq. **4**) in the upper water column, then Eqs. **2** and **4** add to give Eq. **3**, where the expected ratio of $Fe(OH)_3/CH_2O$ delivered from the chemocline is 4/1 (43, 82). If this organic matter is effectively reduced again by Fe reduction (Eq. **1**), then 4 moles of Fe(II) are produced for each mole of HCO_3^- generated from organic matter oxidation. If all of the Fe (II) is precipitated as siderite (Eq. **5**), then only one of the 4 moles of Fe(II) from Fe reduction can be precipitated from organic matter-derived HCO_3^- (82), and the remaining HCO_3^- must come from the general marine reservoir (82). Such a distribution of HCO_3^- sources has isotopic consequences, especially if siderite precipitation occurs in the sediments where the ^{13}C-depleted HCO_3^- (derived from organic-matter mineralization) can accumulate (Fig. 8) (43, 82).

Thus, assuming $\delta^{13}C$ values of 0‰ for seawater HCO_3^- (82) and −32‰ for organic matter-derived HCO_3^- (the same as the kerogen; Fig. 6), then a $\delta^{13}C$ of −8‰ ($3/4 \times 0‰ + 1/4 \times -32‰ = 8‰$) would be consistent with siderite deposition resulting from a balanced organic matter–iron cycle as depicted above (82). The Xiamaling Formation siderites are much more ^{13}C-depleted than this, demonstrating a much larger contribution of organic matter-derived HCO_3^- to the carbonates than expected from a simple iron cycle generating siderite Fe(II) in a 4/1 ratio to organic carbon

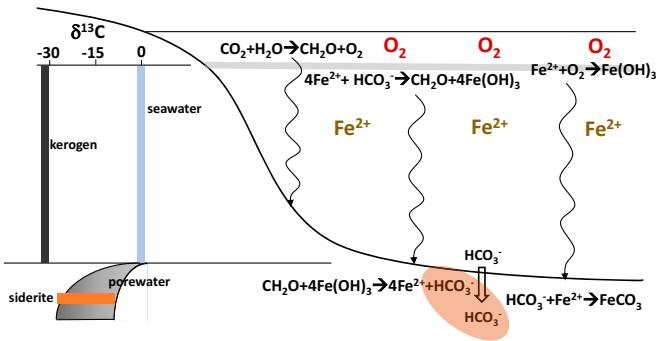

Fig. 7. Cartoon illustrating the Fe cycle active during deposition of the IFs in the Xiamaling Formation unit 5. Shown are the microbial and biological processes active in the water column and in the sediments. Also shown is a sketch demonstrating how the $\delta^{13}C$ of HCO_3^- may have developed in the water column and in the pore waters relative to the $\delta^{13}C$ of organic matter (kerogen) and the $\delta^{13}C$ of the siderites preserved in the IF.

mineralization (Fig. 8). There are at least two ways to explain this discrepancy, assuming that most of the siderite precipitation took place in the sediments where respiration products accumulate, generating the most ^{13}C-depleted bicarbonate (outlined generically in Fig. 8). In the first way, the flux ratio of Fe oxides to organic matter to the sediments could have been near 4/1, but a substantial portion of the Fe(II) produced during iron reduction was not retained in the sediment as siderite, but rather was recycled back to the water column, thus reducing the amount of Fe (II) available for siderite precipitation (82). This also requires, however, that a relatively high proportion of the bicarbonate produced during Fe reduction was precipitated and retained as in the sediment. A second way exists if there was a substantial flux of organic matter to the sediments uncoupled from the $Fe(OH)_3$ flux, providing a settling flux of Fe oxides to organic matter in ratio much less than 4/1. For this to work, anoxygenic photosynthesis would be only a secondary source of organic matter to the sediments. Furthermore, the oxygen produced by oxygenic photosynthesis could not have reacted with Fe(II) in proportion to the settling organic matter flux as explained above, implying a net flux of O_2 to the atmosphere or O_2 reaction with reduced species other than Fe(II).

Both explanations would provide a higher proportion of organic matter-derived HCO_3^- to precipitate with siderite than expected by a balanced Fe cycle with an Fe oxide to organic matter flux of 4/1 as described above, and thereby generating the highly ^{13}C-depleted values we observe. We prefer, however, the first explanation. In this case, sufficient Fe oxides would have been delivered to the sediment to drive organic matter oxidation, by Fe reduction, to the low organic matter concentrations we observe (Fig. 5). But, diffusive loss of Fe(II) from the sediment would have limited the amount of siderite that formed, thus allowing higher proportions of ^{13}C-depleted diagenetic carbonate to precipitate as siderite. The second explanation can produce highly ^{13}C-depleted carbonates due to the overabundance of organic matter, but would also be expected to produce elevated organic carbon concentrations that we do not observe (Fig. 5). Other organic matter mineralization processes such as methanogenesis could have reduced the organic carbon concentrations below what would be expected from Fe reduction alone. Methanogenesis, however, is not very efficient in organic matter mineralization (76) and thus unlikely to have played a large role in influencing organic matter concentrations in these sediments.

Thus, while we prefer an explanation favoring a near 4/1 flux ratio of Fe oxides to organic matter to unit 5 sediments, was anoxygenic photosynthesis responsible for generating this flux ratio? As described above, this observation would be consistent with the presence of TMAIs in the sediments and a primary anoxygenic photosynthetic source for Fe oxides and organic matter. However, the concentrations of TMAIs are low, and, also, the $\delta^{13}C$ of the organic matter (Fig. 6) is much more depleted than the −10 to −15‰ as might be expected from anoxygenic photosynthesis by GSBs alone (76, 84).

Therefore, we suggest a scenario where the fluxes of organic matter and Fe oxides to the sediments were not all directly coupled through anoxygenic photosynthesis. Our observations on the nature of the Fe enrichments show that enhanced Fe deposition was not continuous, but periodic (Fig. 4 and Fig. S1). If enhanced Fe deposition is related to upwelling, for example, then both the nutrients driving primary production by oxygenic photosynthesis and the Fe(II) supplied for Fe deposition could be delivered simultaneously from Fe(II) and nutrient-enriched deep waters, and primary production might be concentrated at the chemocline. In this scenario, a major proportion of the oxygen produced during oxygenic photosynthesis reacted with Fe(II) at the chemocline, coupling the depositional flux of Fe and organic matter. We emphasize, however, that while oxygenic photosynthesis coupled with aerobic Fe(II) oxidation could explain

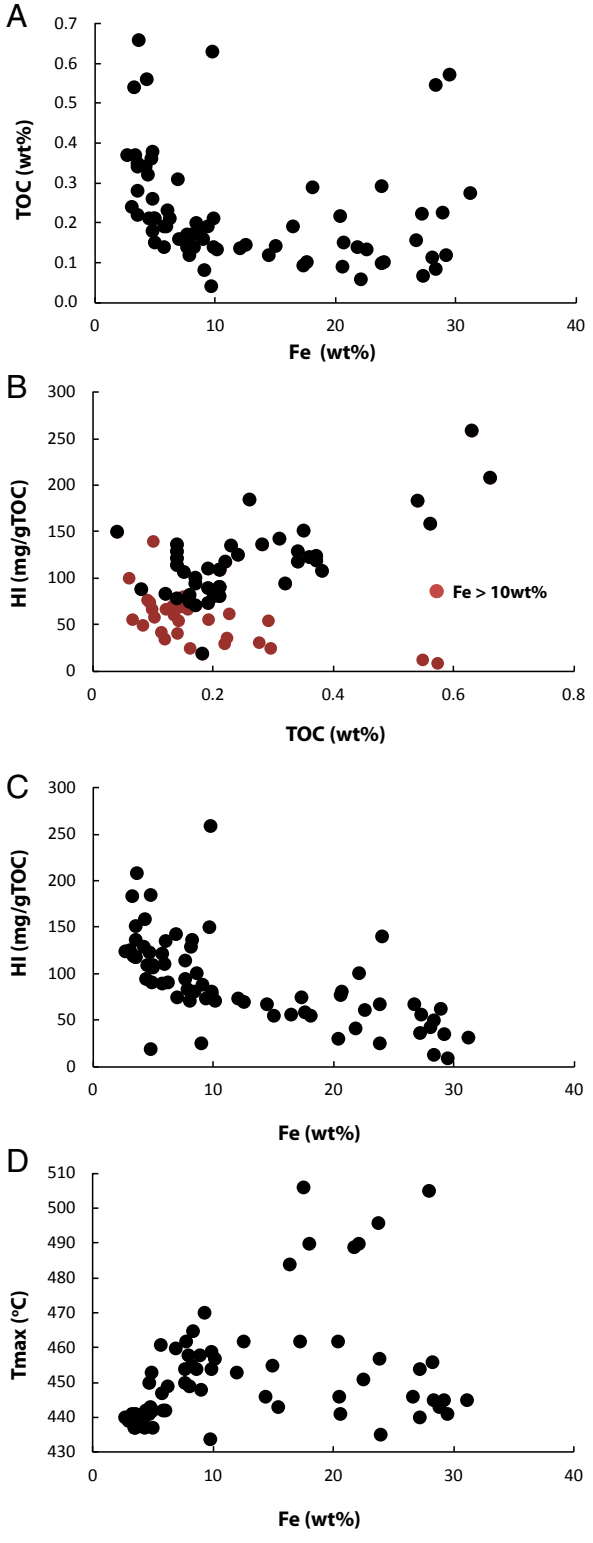

Fig. 8. (*A*) Relationship between total Fe and TOC. (*B*) Relationship between TOC and HI for low Fe (<10 wt%; black dots) and high Fe (>10 wt%) samples from unit 5 of the Xiamaling Formation. (*C*) Relationship between total Fe concentration and HI for unit 5 of the Xiamaling Formation. (*D*) Relationship between total Fe concentration and Tmax, where Tmax is the temperature of the S2 peak maximum during Rock Eval pyrolysis.

our geochemical results, it requires a long-term coupling between the settling fluxes of iron oxides and organic matter to a 4/1 ratio. We have suggested a coupling through upwelling events, but overall, the processes driving the coupling between the Fe oxide and organic matter fluxes are not clear.

Different clues as to the coupling between the carbon and iron cycles come from relationships between total organic carbon content (TOC), Fe, and the hydrogen index (HI), where HI is an indicator of organic matter preservation (85–87). Typically, in sediments of low maturity, TOC and HI show a positive (although not necessarily linear) relationship, where low-TOC samples generally have low HI values. Such samples are usually viewed to have undergone more extensive degradation during diagenesis than high-TOC, high-HI samples (e.g., refs. 85, 87, and 88). We observed the typical pattern between TOC and HI in the relatively low-Fe (<10 wt% Fe) sediments of unit 5 (Fig. 8*B*). Remarkably, the high-Fe sediments (>10 wt% Fe) showed an opposite trend (Fig. 8*B*), where HI decreased with increasing concentrations of TOC. We are unaware of any other sediments showing such a trend. We are confident that this trend does not reflect carbonate interferences during Rock-Eval determination of HI, as carbonates should not interfere with S2 peak from which HI is calculated (see further details in *SI Materials and Methods*). We also observed a strong inverse correlation between HI and Fe content (Fig. 8*C*), suggesting that the organic matter became more decomposed as Fe concentration increased. This relationship does not likely reflect differences in organic matter source, as neither the $\delta^{13}C$ nor $\delta^{15}N$ of kerogen correlate with Fe content, nor does Tmax (Fig. 8*D*). We note that Tmax is highly variable in the unit, and this variability could reflect contributions of organic matter from mass flow events. The variability, however, is independent of Fe concentration and seems to influence all sediments equally, regardless of Fe concentration.

The relationship between Fe abundance and HI, therefore, does not likely result from a different source of degraded organic matter to the Fe-enriched sediments and is more likely a product of early diagenesis. The low values of HI at high Fe concentrations would suggest that Fe reduction can be extremely efficient in organic matter oxidation—indeed, as efficient as oxic respiration when the Fe oxides are supplied in sufficient quantities. Several studies have shown that extensive oxic respiration substantially reduces organic matter preservation, generating sediments with low HI (e.g., refs. 13 and 88–90), whereas the documentation of such extensive carbon mineralization during Fe reduction is lacking. We do note, however, that when Fe oxides are relatively abundant, Fe reduction, accompanied by the related processes of organic matter hydrolysis and fermentation, can be the dominant pathway of anaerobic mineralization in modern marine sediments (91, 92). Furthermore, fresh Fe oxyhydroxides, of the type produced during Fe^{2+} oxidation at neutral pH (21, 93), should be the most reactive phases driving microbial dissimilatory Fe reduction (76, 94). We add that the populations of microbes responsible for Fe reduction can seemingly oxidize a wide range of organic compounds, including aromatics and hydrocarbons not normally thought to be accessible to anaerobic metabolism (95). Finally, ref. 43 has calculated that, although the organic carbon content of Archean BIFs is low (typically 0.01–0.1 wt%), from mass balance considerations, the original TOC content was as high as 1–10 wt%. If correct, these results also point to substantial organic matter mineralization under the ferruginous conditions of late Archean BIFs.

Final Remarks

We report here on an ∼1,400-Ma IF of substantial size within the Xiamaling Formation of the North China Craton. This IF is not well laminated and thus not a BIF, but it nonetheless bears similarities to well-known late-Archean siderite-facies BIFs from South Africa and Australia. In particular, the Xiamaling Formation

IF displays an active iron cycle where iron oxides were deposited together with organic matter and where virtually all of the iron oxides were subsequently reduced during microbial dissimilatory iron reduction. This process of iron reduction appears to have been of similar efficiency to oxic respiration, degrading the organic matter to a poor state of preservation. Such an efficient anaerobic iron cycle has been inferred, but not demonstrated, for BIFs of the Archean Eon. We also found a role for anoxygenic photosynthesis in iron oxide production at the chemocline, but it is unclear whether anoxygenic photosynthesis was the dominant mode of Fe(II) oxidation and subsequent source of iron oxide and organic matter delivery from the chemocline to the sediments.

Overall, we show that substantial IFs did form during the Mesoproterozoic Era. Such Mesoproterozoic-aged IFs did not, however, seem to have been common. The oceans during this time in Earth history supported a mix of sulfidic, ferruginous, and even oxic conditions (10, 11, 13, 14, 17, 96). The distribution of these conditions is uncertain, but a statistical treatment of the available Fe speciation data suggests that euxinic conditions were relatively common during the Mesoproterozoic Era (96). Euxinic conditions provide a strong sink for Fe(II), potentially reducing Fe(II) availability compared with the Archean Eon and the Early Paleoproterozoic Era, where, due to a low-oxygen atmosphere, sulfate was less available from weathering on land to drive sulfide production by sulfate reduction (6, 97). With less sulfide available, marine-dissolved Fe^{2+} concentrations were likely much higher, allowing more IF deposition (37).

Still, occasionally, such as recorded in the Xiamaling Formation, geochemical conditions (with perhaps hydrothermal Fe input) conspired to allow substantial IF deposition, even during times when sulfide was generally more common, and Fe^{2+} relatively less so. Overall, the Xiamaling Formation IF helps fill one of the longest gaps in Earth history where IFs were thought absent from the geologic record and provides an unprecedented view of the dynamics of Fe cycling in IF formation.

Materials and Methods

Samples for geochemical analysis were obtained from fresh drill core, with fresh water used as the drilling fluid to minimize contamination. High-resolution scanning of an IF section was conducted by using an ITRAX μXRF core scanner (COX Analytical Systems 2011). Major element analysis was performed with μXRF (PW2404; Philips Electronics), while trace metal concentrations were determined with an inductively coupled plasma mass spectrometer (Finnigan MAT, Element I). XRD analysis was performed with a Rigaku MiniFlex X-ray diffractometer using a 600 W Cu-kα source. TOC concentrations were measured both with a LECO CS-230HC carbon–sulfur analyzer and through Rock Eval pyrolysis, from which data for HI was also obtained. Kerogen was concentrated from HCl- and HF-treated samples, and the C and N isotopic composition of these samples, as well as the isotopic composition of C and O in carbonates, was determined by mass spectrometry with either a Delta V Advantage mass spectrometer (Thermo Scientific) or a Finnigan Mat-252 mass spectrometer (Thermo Scientific). Hydrocarbons for biomarker analysis were extracted from fresh core material, and in some samples, both inside and outside pieces of core were extracted. See *SI Materials and Methods* for a full description of the methods.

ACKNOWLEDGMENTS. We thank Dina Holmgaard Skov and Heidi Grøn Jensen for expert technical assistance; and Marie-Louise Siggaard-Andersen and Kurt Kjær at the Natural History Museum of Denmark, University of Copenhagen, for access to and skilled guidance of the ITRAX core XRF scanner. This work was supported by Villum Foundation Grant 16518; the 1000 Scientist program of China; Strategic Priority Research Program of the Chinese Academy of Sciences Grant XDA14010101; State Key National Natural Science Foundation of China Grant 41530317; National Science and Technology Major Project Grant 2016ZX05004-001; and Scientific Research and Technological Development Project of China National Petroleum Corporation Grants CNPC 2016A-0204 and 2016A-0205.

1. Bekker A, et al. (2010) Iron formation: The sedimentary product of a complex interplay among mantle, tectonic, oceanic, and biospheric processes. *Econ Geol* 105: 467–508.
2. James HL (1983) Distribution of banded iron-formation in space and time. *Iron-Formation: Facts and Problems*, eds Trendall AF, Morris RC (Elsevier Science, Amsterdam), pp 471–490.
3. Holland HD (1984) *The Chemical Evolution of the Atmosphere and Oceans* (Princeton Univ Press, Princeton), p 582.
4. Isley AE, Abbott DH (1999) Plume-related mafic volcanism and the deposition of banded iron formation. *J Geophys Res* 104:15461–15477.
5. Holland HD (1994) Early Proterozoic atmospheric change. *Early Life on Earth*, ed Bengtson S (Columbia Univ Press, New York), pp 237–244.
6. Canfield DE (1998) A new model for Proterozoic ocean chemistry. *Nature* 396: 450–453.
7. Bekker A, et al. (2004) Dating the rise of atmospheric oxygen. *Nature* 427:117–120.
8. Farquhar J, Bao H, Thiemens M (2000) Atmospheric influence of Earth's earliest sulfur cycle. *Science* 289:756–759.
9. Poulton SW, Fralick PW, Canfield DE (2010) Spatial variability in oceanic redox structure 1.8 billion years ago. *Nat Geosci* 3:486–490.
10. Poulton SW, Canfield DE (2011) Ferruginous conditions: A dominant feature of the ocean through Earth's history. *Elements* 7:107–112.
11. Guilbaud R, Poulton SW, Butterfield NJ, Zhu M, Shields-Zhou GA (2015) A global transition to ferruginous conditions in the early Neoproterozoic oceans. *Nat Geosci* 8: 466–470.
12. Shen Y, Canfield DE, Knoll AH (2002) Middle Proterozoic ocean chemistry: Evidence from the McArthur basin, Northern Australia. *Am J Sci* 302:81–109.
13. Wang X, et al. (2017) Oxygen, climate and the chemical evolution of a 1400 million year old tropical marine setting. *Am J Sci* 317:860–899.
14. Canfield DE (2014) Proterozoic atmospheric oxygen. *Treatise on Geochemistry, Atmosphere-History*, ed Farquhar J (Elsevier, Amsterdam), 2nd Ed, Vol 13.
15. Sperling EA, et al. (2015) Statistical analysis of iron geochemical data suggests limited late Proterozoic oxygenation. *Nature* 523:451–454.
16. Gilleaudeau GJ, Kah LC (2015) Heterogeneous redox conditions and a shallow chemocline in the Mesoproterozoic ocean: Evidence from carbon-sulfur-iron relationships. *Precambrian Res* 257:94–108.
17. Planavsky NJ, et al. (2011) Widespread iron-rich conditions in the mid-Proterozoic ocean. *Nature* 477:448–451.
18. Garrels RM, Perry EA, Jr, Mackenzie FT (1973) Genesis of Precambrian iron-formations and the development of atmospheric oxygen. *Econ Geol* 68:1173–1179.
19. Hartman H (1984) *The Evolution of Photosynthesis and Microbial Mats: A Speculation on the Banded Iron Formations. Microbial Mats: Stromatolites* (Alan R. Liss, Inc., New York), pp 449–453.
20. Widdel F, et al. (1993) Ferrous iron oxidation by anoxygenic phototrophic bacteria. *Nature* 362:834–835.
21. Posth NR, Canfield DE, Kappler A (2014) Biogenic Fe(III) minerals: From formation to diagenesis and preservation in the rock record. *Earth Sci Rev* 135:103–121.
22. Posth NR, Hegler F, Konhauser KO, Kappler A (2008) Alternating Si and Fe deposition caused by temperature fluctuations in Precambrian oceans. *Nat Geosci* 1:703–708.
23. Kappler A, Pasquero C, Konhauser K, Newman DK (2005) Deposition of banded iron formations by phototrophic Fe(II)-oxidizing bacteria. *Geology* 33:865–868.
24. Konhauser K, Newman D, Kappler A (2005) The potential significance of microbial Fe (III) reduction during deposition of Precambrian banded iron formations. *Geobiology* 3:167–177.
25. James HL (1966) Chemistry of the iron-rich sedimentary rocks (US Geological Survey, Reston, VA), US Geological Survey Professional Paper 440-W.
26. Beukes NJ, Klein C (1990) Geochemistry and sedimentology of a facies transition-from microbanded to granular iron formation-in the early Proterozoic Transvaal Supergroup, South Africa. *Precambrian Res* 47:99–139.
27. Ayres D (1972) Genesis of iron-bearing minerals in banded iron formation mesobands in the Dales Gorge member, Hamersley Group, Western Australia. *Econ Geol* 67:1214–1233.
28. Ewers WE, Morris RC (1981) Studies of the Dales Gorge member of the Brockman iron formation, Western Australia. *Econ Geol* 76:1929–1953.
29. Ewers WE (1983) Chemical factors in the deposition and diagenesis of banded iron-formation. *Iron-Formation: Facts and Problems*, eds Trendall AF, Morris RC (Elsevier Science, Amsterdam), pp 491–512.
30. Trendall AF, Blockey J (1970) *The Iron Formations of the Precambrian Hamersley Group, Western Australia with Special Reference to the Associated Crocidolite* (Geological Survey of Western Australia., East Perth, Australia), p 366.
31. Cloud P (1973) Paleoecological significance of banded iron formation. *Econ Geol* 68: 1135–1143.
32. Klein C, Beukes NJ (1989) Geochemistry and sedimentology of a facies transition from limestone to iron-formation deposition in the early Proterozoic Transvaal Supergroup, South Africa. *Econ Geol* 84:1733–1774.
33. Konhauser KO, et al. (2002) Could bacteria have formed the Precambrian banded iron formations? *Geology* 30:1079–1082.
34. Trendall AF (1970) Iron-formation of the Hamersley group of Western Australia: Type examples of varved Precambrian evaporites. *Earth Sci* 9:257–270.
35. Beukes NJ, Klein C, Kaufman AJ, Hayes JM (1990) Carbonate petrography, kerogen distribution, and carbon and oxygen isotope variation in an early Proterozoic transition from limestone to iron-formation deposition, Transvaal Supergroup, South Africa. *Econ Geol* 85:663–690.
36. Millero FJ, Sotolongo S, Izaguirre M (1987) The oxidation kinetics of Fe(II) in seawater. *Geochim Cosmochim Acta* 51:793–801.
37. Raiswell R, Canfield DE (2012) The iron biogeochemical cycle past and present. *Geochem Perspect* 1:1–220.

38. Emerson D, Fleming EJ, McBeth JM (2010) Iron-oxidizing bacteria: An environmental and genomic perspective. *Annu Rev Microbiol* 64:561–583.
39. Druschel GK, Emerson D, Sutka R, Suchecki P, Luther GW (2008) Low-oxygen and chemical kinetic constraints on the geochemical niche of neutrophilic iron(II) oxidizing microorganisms. *Geochim Cosmochim Acta* 72:3358–3370.
40. Weber KA, Achenbach LA, Coates JD (2006) Microorganisms pumping iron: Anaerobic microbial iron oxidation and reduction. *Nat Rev Microbiol* 4:752–764.
41. Crowe SA, et al. (2008) Photoferrotrophs thrive in an Archean ocean analogue. *Proc Natl Acad Sci USA* 105:15938–15943.
42. Walter XA, et al. (2014) Phototrophic Fe(II)-oxidation in the chemocline of a ferruginous meromictic lake. *Front Microbiol* 5:713.
43. Konhauser KO, et al. (2017) Iron formations: A global record of Neoarchaean to Paleoproterozoic environmental history. *Earth Sci Rev* 172:140–177.
44. Fischer WW, Knoll AH (2009) An iron shuttle for deepwater silica in late Archean and early Paleoproterozoic iron formation. *Geol Soc Am Bull* 121:222–235.
45. Trendall AF (1983) The Hammersley basin. *Iron-formation; Facts and Problems*, eds Trendall AF, Morris RC (Elsevier Science, Amsterdam), pp 69–129.
46. Berner RA (1980) *Early Diagenesis* (Princeton Univ Press, Princeton), p 241.
47. Fischer W, et al. (2009) Isotopic constraints on the late Archean carbon cycle from the Transvaal Supergroup along the western margin of the Kaapvaal Craton, South Africa. *Precambrian Res* 169:15–27.
48. Bekker A, et al. (2014) Iron formations: Their origins and implications for ancient seawater chemistry. *Treatise on Geochemistry* (Elsevier, Oxford), Vol 12, pp 561–628.
49. Hu J, Li Z, Gong W, Hu G, Dong X (2016) Meso-neoproterozoic stratigraphic and tectonic framework of the North China craton. *Main Tectonic Events and Metallogeny of the North China Craton* (Springer, New York), pp 393–422.
50. Meng QR, Wei HH, Qu YQ, Ma SX (2011) Stratigraphic and sedimentary records of the rift to drift evolution of the northern North China Craton at the Paleo- to Mesoproterozoic transition. *Gondwana Res* 20:205–218.
51. Peng P, Liu F, Zhai M, Guo J (2012) Age of the Miyun dyke swarm: Constraints on the maximum depositional age of the Changcheng system. *Chin Sci Bull* 57:105–110.
52. Li H, et al. (2013) Recent advances in the study of the Mesoproterozoic geochronology in the North China Craton. *J Asian Earth Sci* 72:216–227.
53. Su W, et al. (2010) SHRIMP U-Pb dating for a K-bentonite bed in the Tieling Formation, North China. *Chin Sci Bull* 55:3312–3323.
54. Zhang SH, Zhao Y, Santosh M (2012) Mid-Mesoproterozoic bimodal magmatic rocks in the northern North China Craton: Implications for magmatism related to breakup of the Columbia supercontinent. *Precambrian Res* 222:339–367.
55. Zhang SH, Zhao Y, Yang ZY, He ZF, Wu H (2009) The 1.35 Ga diabase sills from the northern North China Craton: Implications for breakup of the Columbia (Nuna) supercontinent. *Earth Planet Sci Lett* 288:588–600.
56. Zhang S, et al. (2015) Orbital forcing of climate 1.4 billion years ago. *Proc Natl Acad Sci USA* 112:E1406–E1413.
57. Li HK, et al. (2009) Zircon and beddeleyite U-Pb dating of basic rock sills intruding Xiamaling Formation, North China. *Geol Bull China* 2009:1396–1404.
58. Zhu X, et al. (2013) [Discovery of siderite concretes in Mesoproterozoic Xiamaling Formation, Jixian section.] *Geol Rev* 59:816–822. Chinese.
59. Zhang K, Zhu X (2013) [Genesis of siderites in the Xiamaling Formation of Jiaxian section and its paleoceanic significance.] *Acta Geol Sinica* 87:1430–1438. Chinese.
60. Zhang K, Zhu X-k (2013) [Basic geological characteristics of the siderite-rich strata in the Xiamaling Formation, Jixian County.] *Acta Petrol Miner* 32:529–537. Chinese.
61. Emerson SR, Huested SS (1991) Ocean anoxia and the concentrations of molybdenum and vanadium in seawater. *Mar Chem* 34:177–196.
62. De Baar HJ, Bacon MP, Brewer PG, Bruland KW (1985) Rare earth elements in the Pacific and Atlantic oceans. *Geochim Cosmochim Acta* 49:1943–1959.
63. Bau M, Dulski P (1996) Distribution of yttrium and rare-earth elements in the Penge and Kuruman iron-formations, Transvaal Supergroup, South Africa. *Precambrian Res* 79:37–55.
64. Planavsky N, et al. (2010) Rare Earth element and yttrium compositions of Archean and Paleoproterozoic Fe formations revisited: New perspectives on the significance and mechanisms of deposition. *Geochim Cosmochim Acta* 74:6387–6405.
65. Derry LA, Jacobsen SB (1990) The chemical evolution of precambrian seawater: Evidence for REEs in banded iron formation. *Geochim Cosmochim Acta* 54:2965–2977.
66. Scott C, Lyons TW (2012) Contrasting molybdenum cycling and isotopic properties in euxinic versus non-euxinic sediments and sedimentary rocks: Refining the paleoproxies. *Chem Geol* 324:19–27.
67. Algeo TJ, Rowe H (2012) Paleoceanographic applications of trace-metal concentration data. *Chem Geol* 324:6–18.
68. Klein C, Beukes NJ (1993) Sedimentology and geochemistry of the glaciogenic Late Proterozoic Rapitan iron-formation in Canada. *Econ Geol Bull Soc* 88:542–565.
69. Goodwin AM, Thode HG, Chou C-L, Karkhansis SN (1985) Chemostratigraphy and origin of the Late Archean siderite-pyrite-rich helen iron formation, Michipicoten Belt, Canada. *Can J Earth Sci* 22:72–84.
70. Pufahl PK, Fralick PW (2004) Depositional controls on Palaeoproterozoic iron formation accumulation, Gogebic Range, Lake Superior Region, USA. *Sedimentology* 51:791–808.
71. French KL, et al. (2015) Reappraisal of hydrocarbon biomarkers in Archean rocks. *Proc Natl Acad Sci USA* 112:5915–5920.
72. Zhang S, et al. (2016) Sufficient oxygen for animal respiration 1,400 million years ago. *Proc Natl Acad Sci USA* 113:1731–1736.
73. Brocks JJ, Summons RE (2004) Sedimentary hydrocarbons, biomarkers for early life. *Treatise on Geochemistry, Biogeochemistry*, eds Holland HD, Turekian KK (Elsevier, Amsterdam), Vol 8, pp 64–115.
74. Lu H, et al. (2015) 2, 3, 6-/2, 3, 4-aryl isoprenoids in Paleocene crude oils from Chinese Jianghan Basin: Constrained by water column stratification. *Energy Fuels* 29:4690–4700.
75. Koopmans MP, Schouten S, Kohnen MEL, Damste JSS (1996) Restricted utility of aryl isoprenoids as indicators for photic zone anoxia. *Geochim Cosmochim Acta* 60:4873–4876.
76. Canfield DE, Thamdrup B, Kristensen E (2005) *Aquatic Geomicrobiology* (Elsevier Academic, London), p 640.
77. Overmann J (1992) Phylum BXI. Chlorobi phy. nov. Family I. "Chlorobiaceae" green sulfur bacteria. *Bergey's Manual of Systematic Bacteriology*, eds Boone DR, Castenholz RW, Garrity GM (Springer, New York), 2nd Ed, Vol I, pp 601–604.
78. Heising S, Richter L, Ludwig W, Schink B (1999) *Chlorobium ferrooxidans* sp. nov., a phototrophic green sulfur bacterium that oxidizes ferrous iron in coculture with a "*Geospirillum*" sp. strain. *Arch Microbiol* 172:116–124.
79. Michard A, Albarede F, Michard G, Minster J, Charlou J (1983) Rare-earth elements and uranium in high-temperature solutions from East Pacific Rise hydrothermal vent field (13 N). *Nature* 303:795–797.
80. Elderfield H, Schultz A (1996) Mid-ocean ridge hydrothermal fluxes and the chemical composition of the ocean. *Annual Review of Earth and Planetary Sciences*, eds Wetherill GW, Albee AL, Burke KC (Annual Reviews, Palo Alto, CA), Vol 24, pp 191–224.
81. Beukes NJ, Klein C, Kaufman AJ, Hayes JM (1990) Carbonate petrography, kerogen distribution, and carbon and oxygen isotope variations in an Early Proterozoic transition from limestone to iron-formation deposition, Transvaal Supergroup, South Africa. *Econ Geol* 85:663–690.
82. Heimann A, et al. (2010) Fe, C, and O isotope compositions of banded iron formation carbonates demonstrate a major role for dissimilatory iron reduction in~2.5 Ga marine environments. *Earth Planet Sci Lett* 294:8–18.
83. Craddock PR, Dauphas N (2011) Iron and carbon isotope evidence for microbial iron respiration throughout the Archean. *Earth Planet Sci Lett* 303:121–132.
84. Posth NR, et al. (2017) Carbon isotope fractionation by anoxygenic phototrophic bacteria in euxinic Lake Cadagno. *Geobiology* 15:798–816.
85. Espitalie J, et al. (1977) Rapid method for source rocks characterization and for determination of petroleum potential and degree of evolution. *Rev Inst Fr Pet* 32: 23–42.
86. Zhang S, et al. (2017) The oxic degradation of sedimentary organic matter 1.4 Ga constrains atmospheric oxygen levels. *Biogeosciences* 14:2133–2149.
87. Pratt LM (1984) Influence of paleoenvironmental factors on preservation of organic matter in Middle Cretaceous Greenhorn Formation, Pueblo, Colorado. *Am Assoc Pet Geol Bull* 68:1146–1159.
88. Bouloubassi I, Rullkötter J, Meyers PA (1999) Origin and transformation of organic matter in Pliocene-Pleistocene Mediterranean sapropels: Organic geochemical evidence reviewed. *Mar Geol* 153:177–197.
89. Pratt LM, Claypool GE, King JD (1986) Geochemical imprint of depositional conditions on organic matter in laminated-bioturbated interbeds from fine-grained marine sequences. *Mar Geol* 70:67–84.
90. Nierop KG, Reichart G-J, Veld H, Damsté JSS (2017) The influence of oxygen exposure time on the composition of macromolecular organic matter as revealed by surface sediments on the Murray Ridge (Arabian Sea). *Geochim Cosmochim Acta* 206:40–56.
91. Canfield DE, et al. (1993) Pathways of organic carbon oxidation in three continental margin sediments. *Mar Geol* 113:27–40.
92. Thamdrup B (2000) Bacterial manganese and iron reductin in aquatic sediments. *Microbial Ecology*, ed Schink B (Kluwer Academic, Plenum, New York), Vol 16, pp 41–84.
93. Kappler A, Newman DK (2004) Formation of Fe(III)-minerals by Fe(II)-oxidizing photoautotrophic bacteria. *Geochim Cosmochim Acta* 68:1217–1226.
94. Canfield DE (1989) Reactive iron in marine sediments. *Geochim Cosmochim Acta* 53:619–632.
95. Lovley DR, Holmes DE, Nevin KP (2004) Dissimilatory Fe(III) and Mn(IV) reduction. *Adv Microb Physiol* 49:219–286.
96. Sperling EA, et al. (2014) Redox heterogeneity of subsurface waters in the Mesoproterozoic ocean. *Geobiology* 12:373–386.
97. Cameron EM (1982) Sulphate and sulphate reduction in Early Precambrian oceans. *Nature* 296:145–148.
98. Rudnick RL (2004) Composition of the continental crust. *Treatise on Geochemistry: The Crust*, ed Rudnick RL (Elsevier, Amsterdam), Vol 3, pp 1–64.